https://doi.org/10.1590/jatm.v18.1429 ORIGINAL PAPER

Study on the Thermal Stress and Thermal Deformation of the Grids for an Ion Thruster

Fanting Kong[1], Mingming Sun[1,2,*], Yaotong Ma[1]

1. Lanzhou University of Arts and Sciences – School of Media Engineering – Lanzhou/Gansu – China.
2. China Academy of Space Technology – Lanzhou Institute of Physics – Science and Technology on Vacuum Technology and Physics Laboratory – Lanzhou/Gansu – China.

***Corresponding author:** smmhappy@163.com

ABSTRACT

The structural stability of the grids has a significant influence on the work performance of ion thrusters. To obtain the thermal deformation of the grids for a 30 cm diameter ion thruster, the structural properties of the grids are equivalently analyzed by material mechanics, and the equivalent results are verified. The finite element method is used to study the distribution of thermal stress and thermal deformation of the grids, and the simulation results indicate that, after the equivalent treatment of the grids, the equivalent Young's modulus of the screen grid and the accelerator grid are 20.792 GPa and 89.435 GPa, respectively. When the grids are equivalently treated as a circular plate and the edge is not constrained, the maximum thermal deformation of the grids caused by tensile stress is 0.311 mm, and the maximum thermal stress is about 1.512×10^6 Pa, which occurs in the center of the grids. When the grid is equivalently treated as a circular plate and the edge is constrained, the maximum deflection occurs in the geometric center of the circular plate. Moreover, the maximum deflection of the screen grid is about 1.145 mm, and that of the accelerator grid is about 0.665 mm; the relative distance variation between the screen grid and the accelerator grid is 0.480 mm. The hot gap test is conducted after the thruster has been operated stably for 2 hours without beam extraction. By comparing with the initial gap of the grids, the test results show that the gap variation between the screen grid and the accelerator grid is in the range of 0.502 ~ 0.553 mm. The compare results show that the theoretical results are in good agreement with the experimental results, which also proves the accuracy of the equivalent structural properties of the grids.

Keywords: Ion accelerators; Thermal analysis; Thermal deformation; Thermal stress.

INTRODUCTION

With the increasing requirements for in-orbit application of ion thrusters, the structural stability of the thrusters under extreme environments (such as vibrations during rocket launch, extreme high and low temperatures, and dynamic impacts) has been given more attention (Liu *et al.* 2007). The grids are the most important component of an ion thruster, but their structural stability is the weakest. Meanwhile, the grids have the greatest difficulty in the structural analysis for an ion thruster (Mueller *et al.* 1995; Sun and Qi 2023). During the operation of the thruster, the discharge chamber accumulates a large amount of heat, which is conducted and radiated toward the grids, causing a high temperature of the grids (Wen *et al.* 2011). In addition, due to the ion beam focusing characteristics of the grids, which lead to a higher temperature in the geometric center and a lower temperature at the edge of the grids (MacRae *et al.* 1982), a large temperature difference is caused along the radial direction of the grids. Thermal stresses produced by the non-uniform temperature distribution can cause structural buckling and edge warping of the grids under

Received: Nov. 14, 2025 | **Accepted:** Jan. 16, 2026
Peer Review History: Single Blind Peer Review.
Section editor: Marcia Mantelli

CC BY

different boundary restraints (Goebel and Katz 2008; Haag and Soulas 2002). A 30 cm diameter ion thruster is designed for the Chinese new generation of large truss-type satellite platform (Sun *et al.* 2014). However, since the rated working power of the 30 cm diameter ion thruster is up to 5 kW, the grids will have a higher temperature and greater thermal deformation, which can lead to a short circuit between the grids or changes in beam focusing ability caused by deformation of the grids. Therefore, studying the structural stability of the grids is of great significance for enhancing the reliability of ion thrusters.

Meckel *et al.* (2004) conducted a structural analysis of the C-C (carbon-carbon) grids (with the opening rates of 66% and 24% for the screen grid and the accelerator grid, respectively) of an ion thruster. Since it was practically impossible to conduct a mechanical analysis on grids containing all the apertures. Therefore, a rectangular area with holes was taken from the actual multi-hole plate grid, and this area was equivalently treated as a non-hole plate grid of the same size. After that, based on the finite element method (FEM), multiple iterations of calculations were carried out to compare the actual stress and equivalent stress in the two areas, thereby obtaining the stress concentration factors (which are 5.9 and 2.6 for the screen grid and the accelerator grid, respectively), and the equivalent Young's modulus of the grids was calculated based on these factors. Then the non-hole plate grid with equivalent Young's modulus could replace the actual multi-hole plate grid for structural analysis. Moreover, the results of thermal deformation analysis showed that the center deflections were 22% and 24% of the grid gap for the accelerator grid and the screen grid, respectively. Gao *et al.* (2008) studied the thermal stress distribution of a two-grid system for an ion thruster. The grids were equivalently treated as a plate, and based on the measured temperature in the edge area of the grids, the temperature distribution of the grids was regarded as uniformly distributed. Meanwhile, since the actual grids had a multi-hole structure, Gao *et al.* (2008) introduced a structural strength reduction factor, which was approximately 0.42 by calculation. After equivalent treatment of the actual Young's modulus of the grids, the thermal deformations of the grids were calculated based on temperature variation and thermal stress. Soulas (2006) studied the thermal deformation of an arched multi-hole grid, and the arched multi-hole grid was equivalently treated as a non-hole plate with equivalent Young's modulus. Based on the relationship between thermal deformation and thermal stress, the analytical solutions for the thermal deformation of the equivalent grid were calculated. The error between the FEM result and the analytical solution was 2.94%. Moreover, Soulas and Frandina (2004) and Diaz and Soulas (2006) measured the hot gap variation of a two-grid system by a digital imaging technique. A camera and a microscope were used to capture the real-time position of the probe (fixed to the grids), and image processing was used to calculate the change in position of the probe, thereby measuring the grid gap variation. The previous research mainly focuses on the method of equivalent treatment of the grid structure, and most of the studies adopt the uniformization method of the multi-hole grid structure, with finite element analysis used for verification. This paper systematically investigates the equivalent treatment of the multi-hole grid based on the material mechanics analysis method, and the accuracy of the equivalent process is verified using FEM and experiments.

The analysis process of this paper uses material mechanics analysis and finite element analysis to equivalently analyze the grids of the ion thruster, after which a finite element analysis model is established using software. Moreover, the thermal stress and thermal deformation of the grids under different constraint conditions are obtained by finite element simulation. After that, a hot gap test without beam extraction is conducted to obtain the grid gap variation, and the test results are used to verify the simulation results.

Equivalent treatment of the grids

For the grids of a 30 cm diameter ion thruster, both the thicknesses of the screen grid and the accelerator grid are 0.5 mm, and the curvature height is 12 mm. In addition, there are more than 10,000 holes on the screen grid and the accelerator grid, and the opening rates of the screen grid and the accelerator grid are 69% and 24%, respectively. As shown in Fig. 1, under the influence of non-uniform temperature field, the thermal deformation can cause a series of problems, including short circuits and mounting hole misalignment. Therefore, a study on thermal stress and thermal deformation of the grids is of great significance for improving the reliability of the ion thrusters.

The schematic diagram of the grids for the 30 cm diameter ion thruster is shown in Fig. 2. Because the grids are curved and contain numerous apertures, it is difficult to build an accurate structural model using conventional CAD software. In addition, the distances between each hole are too small to mesh for finite element analysis. To achieve finite element modeling, the grid is approximated as a simple structure without holes, which has the same curvature height as the real structure. Meanwhile, the material properties also need to be equivalently treated; that is, the equivalent elastic modulus of the grids should be obtained first.

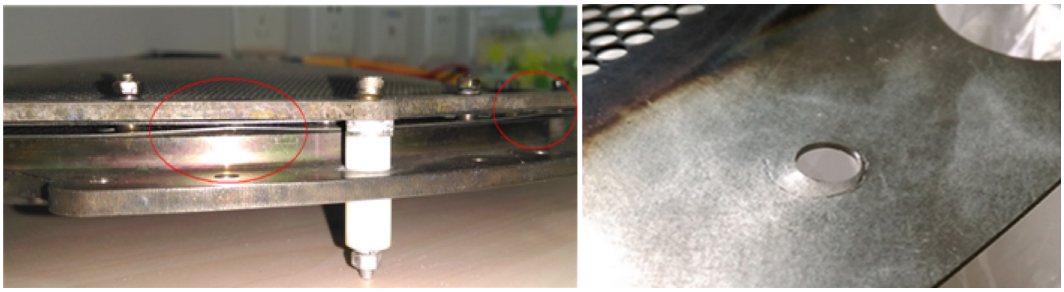

Source: Elaborated by the authors.

Figure 1. Thermal deformation of the grids for a 30 cm diameter ion thruster.

The equivalent elastic modulus of the grids should be calculated in two steps. Firstly, the grids are approximated as uniform plate structures without holes, and the accuracy of the approximate model needs to be verified. After that, the elastic modulus variation under different curvature heights is taken into consideration. As shown in Fig. 2, a single grid aperture can be approximated as a hexagonal structure can be further approximated as a ring structure. In Fig. 2, l is the ring outside diameter, r is the ring inside diameter, and t is the thickness.

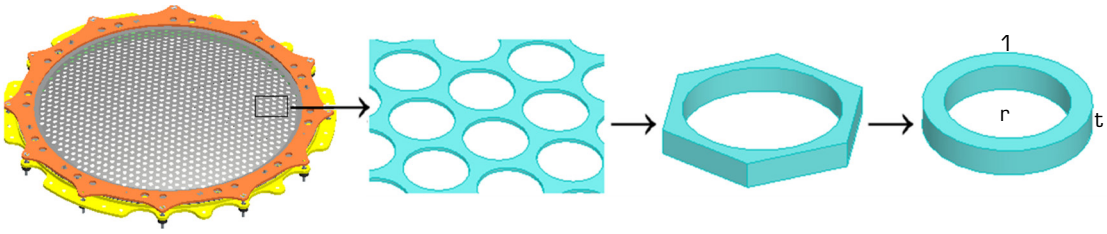

Source: Elaborated by the authors.

Figure 2. Equivalent model of the grids.

According to the calculation model shown in Fig. 3, the equivalent elastic modulus of the grids in y axis is acquired. As shown in Fig. 3 (left), assuming the forces loaded on the structure in y axes at points A and B are P, and the structural deformation is set to be ΔAB, namely the relative displacement between point A and point B, which can be obtained first. Due to the structure and loads being symmetric along the CD axis, cutting the structure from the CD section, and the deformation in y axis can be expressed as $\Delta y_{CD} = 0$, and the rotation angle can be expressed as $\theta = 0$. Considering $F_C = F_D = 0$, and then the bending moment can be expressed as $\tilde{M}_C = \tilde{M}_D = 0$. Meanwhile, the calculation model shown in Fig. 3 (left) can be approximated as what is shown

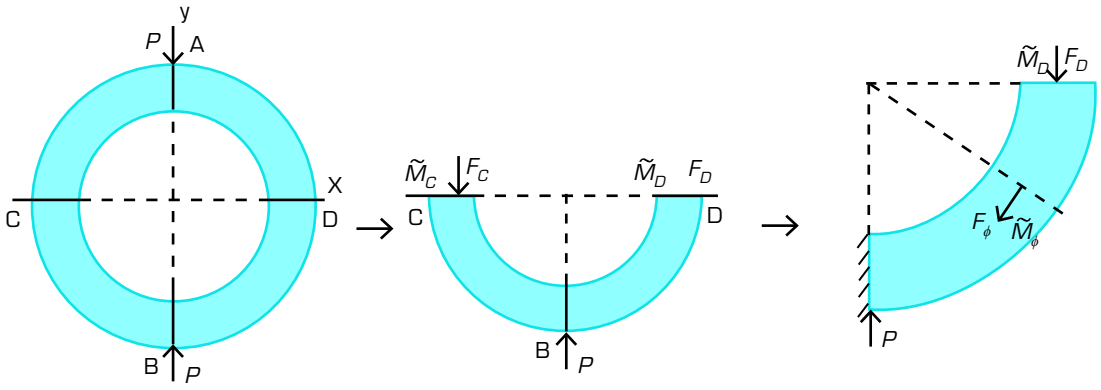

Source: Elaborated by the authors.

Figure 3. Mechanics property analysis for grid aperture.

CC BY

in Fig. 3 (middle), and it is known that $F_D = F_C = P/2$ from the equilibrium condition $\sum F_y = 0$. Due to the structure shown in Fig. 3 (middle), which is also symmetric along the B section, the deformation in x axis and the rotation angle of the B section are both zero. As shown in Fig. 3 (right), the structure in Fig. 3 (middle) is divided into two parts, then the deformation of the B section in y axis can be expressed by the relative displacement between surface A and surface B while fixing the B section. The section ϕ of which the central angle is ϕ shown in Fig. 3 (right) is taken as the research object.

According to the stress balance term, the axial force, which is perpendicular to the section ϕ, is expressed as $F_\phi = F_D \cos\phi$, and the equations $\partial F_\phi / \partial F_D = \cos\phi$ and $\partial F_\phi / \partial \widetilde{M}_D = 0$ could be obtained. The bending moment $\widetilde{M}_\phi$ on section ϕ is acquired under the moment equilibrium condition from Eq. 1:

$$\widetilde{M}_\phi = F_D[r + (l-r)/2](1-\cos\phi) + \widetilde{M}_D \tag{1}$$

The derivatives of $\widetilde{M}_\phi$ are $\partial \widetilde{M}_\phi / \partial F_D = (l+r)(1-\cos\phi)/2$ and $\partial \widetilde{M}_\phi / \partial \widetilde{M}_D = 1$ and the structural strain energy U is defined as Eq. 2:

$$U = \int_0^{\pi/2} \frac{F_\phi^{\,2}}{2EA}\left(\frac{l+r}{2}\right)d\phi + \int_0^{\pi/2} \frac{\widetilde{M}_\phi^{\,2}}{2EI}\left(\frac{l+r}{2}\right)d\phi \tag{2}$$

where E is the real elastic modulus (about 320 GPa) of the grids, A and I are the section area and inertial moment of the ring, respectively, and are defined as $A = (l-r)t$ and $I = (l-r)^3 t/12$ in the paper, *EA* and *EI* are the tensile rigidity and flexural rigidity. Regarding the structure as a linear elastic body, Eqs. 3 and 4 are obtained by using Castigliano's second law (Haag and Soulas 2003):

$$\frac{\partial U}{\partial \widetilde{M}_D} = \theta_D = 0 \tag{3}$$

$$\frac{\partial U}{\partial F_D} = \Delta BD = \frac{1}{2}\Delta AB \tag{4}$$

By substituting Eq. 2 into Eq. 3, the bending moment of the D section $\widetilde{M}_D$ can be expressed as:

$$\widetilde{M}_D = F_D(2-\pi)(l+r)/2\pi \tag{5}$$

Substituting $\widetilde{M}_D$ into Eq. 1, $\widetilde{M}_\phi$ becomes $\widetilde{M}_\phi = F_D(2/\pi - \cos\phi)(l+r)/2$. Rewriting Eq. 4 as Eq. 6 in integral form, and substituting the parameters in Eq. 6, then the structural deformation ΔAB becomes:

$$\Delta AB = \int_S \frac{F_\phi \partial F_\phi / \partial F_D}{EA} dS + \int_S \frac{\widetilde{M}_\phi \partial \widetilde{M}_\phi / \partial \widetilde{M}_D}{EI} dS = \frac{\pi F_D (r+l)}{8EA} \tag{6}$$

By using the relation between stress σ and strain ε (F_D and ΔAB are stress and strain, respectively), the elastic modulus in y axis can be expressed as Eq. 7:

$$E_y = \sigma_y / \varepsilon_y = 8E(l-r)/\pi(l+r) \tag{7}$$

CC BY

Assuming that the material of the equivalent model is isotropic, the equivalent elastic modulus E_{eff} of the grids can be expressed as Eq. 8:

$$E_{eff} = E_x = E_y \tag{8}$$

To verify the accuracy of the equivalent results, the finite element simulation using ANSYS software is adopted for comparison. A perforated plate model with the same material properties, hole size, and thickness as the actual grids, and an imperforated plate model using equivalent material properties, but the same size and thickness as the perforated plate model, are established, respectively. By applying an external force of 10 N in the opposite directions at the upper and lower boundaries of the two models, the deformation results of the two models are shown in Fig. 4. According to the simulation results, the deformations of the two models are basically the same, while the deformation of the equivalent structure is larger. The error mainly results from the assumption that the grid structure is equivalently treated as a ring. Based on the simulation results, the equivalent elastic modulus of the grids with curvature height is considered next.

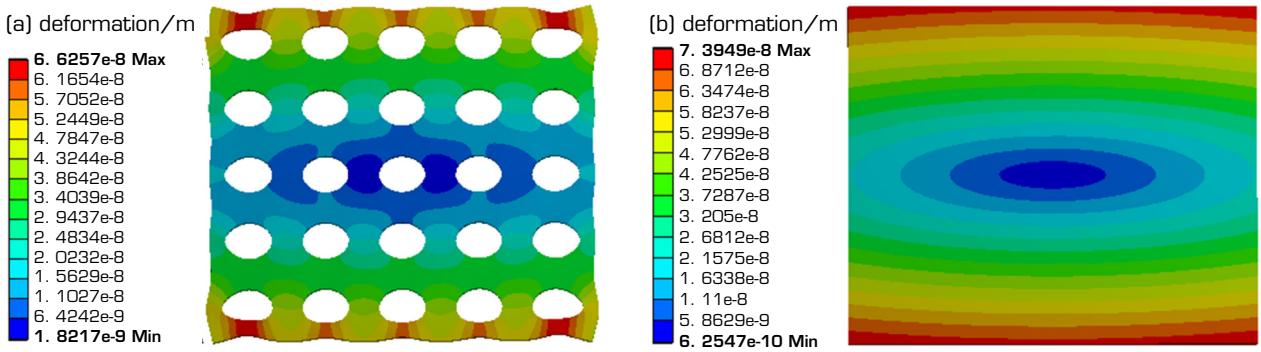

Source: Elaborated by the authors.

Figure 4. Comparison of actual deformation and effective deformation for two models. (a) deformation of the model with aperture; (b) deformation of the non-aperture model.

There are two appropriate ways to consider the influence of the grid curvature height: using the theory of material mechanics or calculation using FEM. In this paper, the elastic modulus of the grids is calculated by the material mechanics method, and the influence of the curvature height on the elastic modulus is estimated by the FEM method. Models of the grids with different curvature heights of 4 mm, 8 mm, 12 mm, and 16 mm are built, respectively. According to the theory of material mechanics, when the size ratio of microstructure (aperture diameter) and macrostructure (grid diameter) is less than 10^{-2} (in this paper, the ratios are 3×10^{-3} and 4.5×10^{-3} with respect to the screen grid and the accelerator grid), then the elastic modulus of the vaulted structure can be set as the elastic modulus of an equivalent plate (Hassani and Hinton 1999a; b). Then, an external force of 10 N in the opposite directions along the diameter direction is applied to the grid, and 80 evenly spaced sampling points in the diameter direction (direction of the applied external force) are selected. According to the stress and strain simulated at these 80 points, the elastic modulus of each point can be obtained, and the elastic modulus of the grids is represented as the average value of the elastic modulus of the 80 points. The deformations with curvature heights of 8 mm and 12 mm are shown in Fig. 5, respectively.

The calculated elastic modulus of the screen grid and the accelerator grid with different curvature heights is shown in Table 1.

According to the calculated results shown in Table 1, the elastic modulus of the grids decreases with increasing curvature height, and the variation of the elastic modulus decreases and tends to be stable when the curvature height increases to a certain extent. For the 30 cm diameter ion thruster, the elastic modulus of the screen grid and the accelerator grid with a curvature height of 12 mm are 20.792 GPa and 89.435 GPa, and the equivalent coefficients are 0.741 and 0.192, respectively.

CC BY

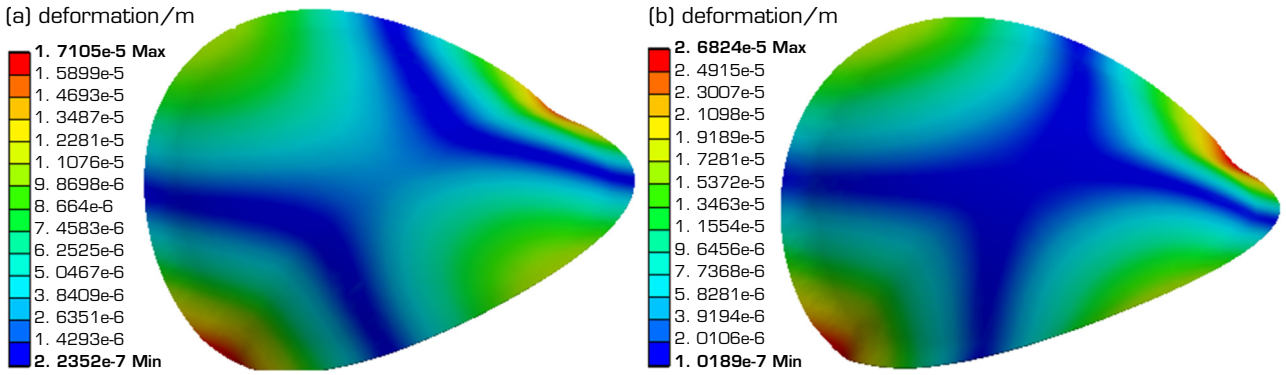

Source: Elaborated by the authors.

Figure 5. Comparison of deformation for different curvature heights of the grids. (a) deformation of 8 mm curvature height; (b) deformation of 12 mm curvature height.

Table 1. The calculated elastic modulus of the grids.

Curvature height (mm)	The screen grid Young's modulus (GPa)	The accelerator grid Young's modulus (GPa)
Flat grids	59.654	236.801
4	37.422	155.046
8	27.522	113.357
12	20.792	89.435
16	21.024	87.128

Source: Elaborated by the authors.

The equivalent density of the grids should be taken into consideration after obtaining the equivalent elastic modulus. The equivalent densities of the grids are related to the opening rate R_A, while the multi-hole grid structure is equivalently treated as a flat plate without holes (Hassani and Hinton 1999c). The equivalent method of the grid density for the ion thruster is replaces the original material density ρ with the equivalent density ρ_{eff}, which is shown in Eq. 9, and the equivalent material properties are shown in Table 2.

$$\rho_{\text{eff}} = (1 - R_A)\rho \tag{9}$$

Table 2. The equivalent mechanical properties of the grids.

Components	Material	Opening rate	Density (effective) (kg·m^{-3})	Young's modulus (effective) (GPa)
Screen grid	Molybdenum	0.69	2973.000	20.792
Accelerator grid	Molybdenum	0.27	7001.000	89.435

Source: Elaborated by the authors.

Surface temperature distribution of the grids

When the thruster is operating, the grids are applied with high voltage ranging from 1000 V to 1500 V, and the surfaces of the grids are bombarded and sputtered by ions, making it difficult to use common thermal sensors to measure the temperature of the beam extraction area on the grids. Therefore, only the temperature in the edge area, which is far from the beam extraction area,

can be measured. As the surface temperature distribution of the grids cannot be directly measured, the structure of the grids can be regarded as a flimsy round plate, taking into consideration of the symmetric characteristics of the temperature distribution $T(t,r)$, where t and r are time and radial distance, respectively. The temperature distribution characteristics of the grids are such the temperature in the central area is much higher than that at the edge area, and the temperature diffuses from the center to the edge area, which conforms to the characteristics of spot welding. Therefore, the temperature distribution can be estimated according to the fundamental solution of the one-dimensional heat conduction equation, which is also called the Cauchy problem (Cao *et al.* 2005). The temperature can be expressed as Eq. 10:

$$T(t,r) = \frac{1}{2k\sqrt{\pi t}} \exp\left(-\frac{r^2}{4k^2 t}\right) \tag{10}$$

where λ is thermal conductivity, c is the specific heat capacity, and ρ is the material density, r is the radius of the grid, and the direction is from the center to the edge of the grid (ranging from 0 m to 0.150 m). A temperature measurement test is conducted when the ion thruster is operating under rated working conditions, with a working power of 5 kW. The temperatures in the edge areas of the screen grid and the accelerator grid are measured by thermocouples, as shown in Fig. 6a. Ceramic screws are designed to fix the thermocouples and ensure the insulation between the sensors and the thruster; a thin copper plate is used as the heat conduction plate, and the sensors are installed on the copper plate to complete the measurement. According to the test results, when the surface temperature distribution of the grids reaches thermal equilibrium, the temperatures in the edge areas of the screen grid and the accelerator grid can reach up to 380 °C and 312 °C, respectively. Based on Eq. 10, it can be calculated that the temperatures in the central areas of the screen grid and the accelerator grid are 407 °C and 335 °C, respectively. The temperature distribution of the screen grid is shown in Fig. 6b. Due to the complexity of the fundamental solution, this paper adopts a polynomial to describe the temperature distribution of the grids, which can be expressed as $T(r) = Ar^2 + Br + C$, where A, B, and C are coefficients to be determined.

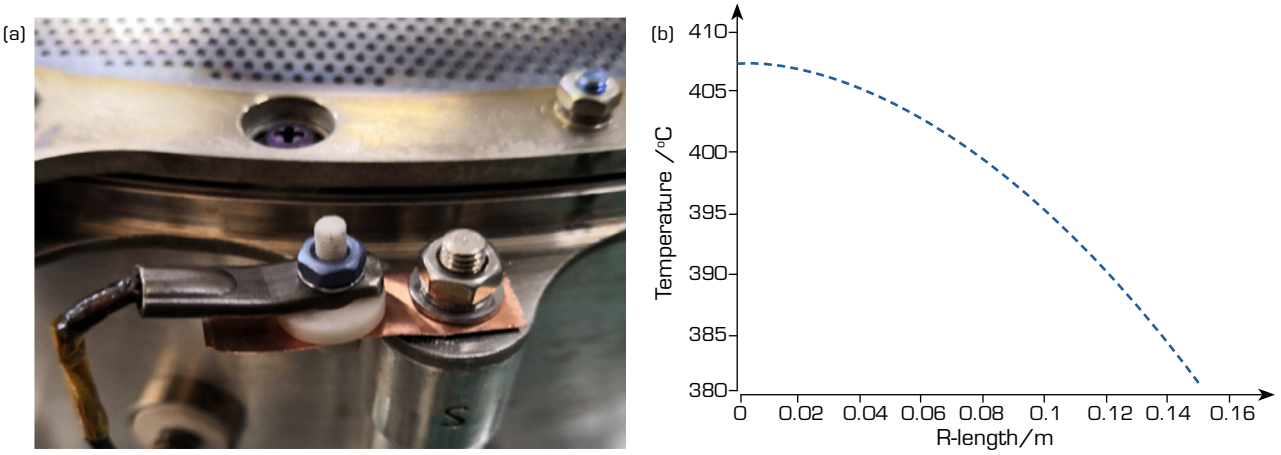

Source: Elaborated by the authors.

Figure 6. Temperature measurement test and calculated temperature distribution of the screen grid. (a) temperature measurement test; (b) calculated temperature of the screen grid (operation time of the thruster is 1,500 s).

Thermal stress of the grids without edge fixed support

According to the equivalent mechanical properties and surface temperature distribution of the grids, the thermal stress and thermal deformation under different fixed statuses of the grids can be analyzed. Before the grid is fixed, the previous thermal treatment process is implemented. Therefore, it is necessary to consider the thermal stress of the grids without edge fixed support first. With the assumption that the grids are well-distributed round boards, the grids can elongate freely on the X-Y plane and

CC BY

displacement in the Z direction or warping will not appear. Therefore, as shown in Eq. 11, the coordination equation of strain is adopted to calculate thermal stress, where Φ is the thermal stress function, and α is the coefficient of thermal expansion:

$$\nabla^4\Phi + \alpha E\nabla^2 T = 0 \tag{11}$$

The stress function Φ can be expressed as $\Phi = U - V$, where U and V represent the stress components in different directions. Substituting $T(r)$ (in fitted form) into Eq. 11, then the stress component V can be obtained by Eq. 12:

$$V = \int_0^r \frac{\alpha E}{r}[\int_0^r rT(r)dr]dr = \frac{A\alpha E}{16}r^4 + \frac{B\alpha E}{9}r^3 + \frac{C\alpha E}{4}r^2 \tag{12}$$

Similarly, based on the equation that $\partial U/\partial r = \partial V/\partial r$, the stress component U can be obtained by Eq. 13, where b is the radius of the grids:

$$U = \int_0^r \frac{\alpha E}{b}\left[\int_0^b rT(r)dr\right]dr = (\frac{A\alpha E}{4}b^3 + \frac{B\alpha E}{3}b^2 + \frac{C\alpha E}{2}b)r \tag{13}$$

According to the two-dimensional radial thermal stress equation, the stress function Φ can be expressed under polar coordinates, and then the radial stress f_r can be obtained by Eq. 14:

$$f_r = \frac{1}{r}\frac{\partial(U-V)}{\partial r} + \frac{1}{r^2}\frac{\partial^2(U-V)}{\partial\theta^2} = \frac{A\alpha E}{4}(b^2 - r^2) + \frac{B\alpha E}{3}(b - r) \tag{14}$$

According to the equation for tangential stress f_θ and stress function Φ. In the same way, tangential stress f_θ can be obtained by Eq. 15:

$$f_\theta = \frac{\partial^2(U-V)}{\partial r^2} = \frac{A\alpha E}{4}(b^2 + r^2) + \frac{B\alpha E}{3}(b + r) + C\alpha E - \alpha E(Ar^2 + Br + C) \tag{15}$$

Taking Eqs. 11-15 into consideration, the direct stress of the grids can be obtained in both radial and tangential directions (Gao *et al.* 2008). Finite element analysis is used to verify the calculation result, and f_i is the resultant of radial stress and tangential stress, which can be expressed as $f_i = \sqrt{f_r^2 - f_r f_\theta + f_\theta^2}$. Taking the screen grid as an example, the diameter of the model is 30 cm, and the thickness is 0.5 mm; the temperatures in the center area and the edge area are 407 °C and 380 °C, respectively. Fig. 7a shows the comparison results of simulated stress and calculated thermal stress of the screen grid, and the radial length ranges from 0 to 0.150 m.

According to Fig. 7a, the calculated maximum stress is in the center area of the grids, and the value reaches up to 1.512×10^6 Pa, while the stress in the middle zone of the grids is the smallest. Meanwhile, the finite element analysis results show that the stress in the center of the grids is close to the theoretical results. However, the stresses in the edge area obtained by the two methods are greatly different, and the calculated values are obviously larger than the simulated ones. The main reason is that the theoretical model is a two-dimensional plane, of which the thickness can be neglected. However, the finite element model is a three-dimensional model; although the thickness is considerably small, it can able to influence the results. In addition, with an increase in the thickness of the model, thermal stress in the edge area tends to decrease. As shown in Fig. 7b, the variation trend of the thermal deformation indicates that the tensile stress in the horizontal direction is the main cause of the deformation.

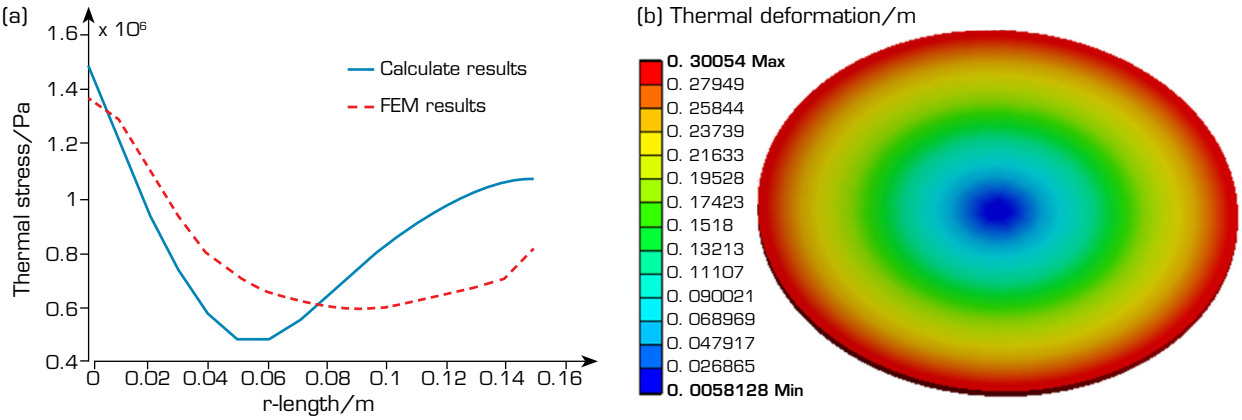

Source: Elaborated by the authors.

Figure 7. Calculation and simulation results of thermal stress and thermal deformation. (a) Comparison of calculation and simulations; (b) thermal deformation of the FEM model.

Thermal stress of the grids with edge fixed support

When the edge of the grids is fixed supported, bending stress and shear stress caused by thermal expansion will lead to structural damage of the grids. The bending moment increases the structural deflection, especially for the structure of a circular plate with fixed support. Tensile stress leads to the expansion of the circular structure at the edge. As the edge is fixed and supported, stress in the fixed area is much greater than that in other areas; that is, the fastening components are subjected to severe yield stress. Shear displacement caused by thermal stress results in a reduction in the rigidity of the whole structure. The schematic of stress on the grids with edge fixed support is shown in Fig. 8. The initial structure of the grids can be treated as a flat plate, which bends under the influence of thermal stress. As shown in Fig. 8, the compressive stress tends to increase the displacement in the Z direction.

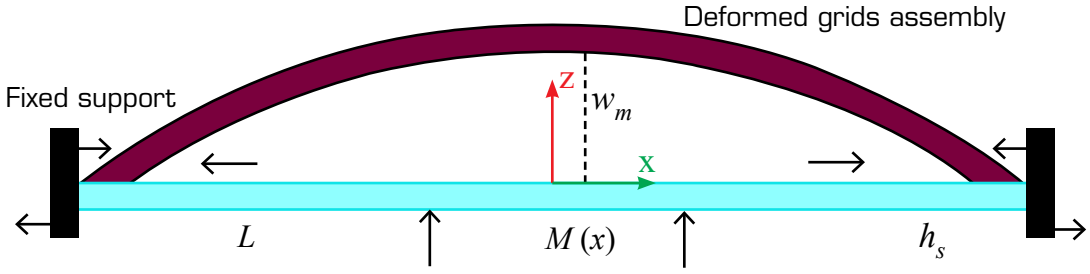

Source: Elaborated by the authors.

Figure 8. Thermal stress of the grids with edge fixed support.

It should be noted that the bending moment causes the deflection of the plate. According to the bending moment equation shown in Eq. 16, where w and f are the deflection and stress of the structure, respectively, the corresponding bending moment is $M(x)$:

$$M(x) = \int_A wf\mathrm{d}A = \int_0^b \alpha ET(r)h_s r\mathrm{d}r \tag{16}$$

Assuming that all the edges of the grids are fixed and supported and that no rotation has occurred, it can be concluded that the torsional moment is 0, that is $N = 0$. Then, the deformation of the structure depends only on the influence of the bending moment. According to the differential equation of deflection, which is shown in Eq. 17, where E is the bending rigidity:

CC BY

$$\frac{\mathrm{d}^2 w}{\mathrm{d}x^2} = -\frac{M(x)}{E} \tag{17}$$

The maximum deflection w_m is taken into consideration. As the temperature in the center area is the highest, the deflection in this area is the maximum. Substituting the fitted temperature distribution into Eq. 17, the maximum deflection w_m can be expressed as Eq. 18, and the inertia moment I can be expressed as $I = h_s b^3/12$:

$$w_m = \frac{ML^2}{8EI} = \frac{\alpha h_s b^2}{2I}\left(\frac{Ab^4}{4} + \frac{Bb^3}{3} + \frac{Cb^2}{2}\right) \tag{18}$$

After the expression of the deflection is obtained, the maximum elongation caused by tensile stress should be calculated. The maximum elongation is equal to the elongation brought by deflection. According to the study results by Gatewood (1957), the maximum elongation caused by thermal stress ΔL can be expressed as Eq. 19, where L represents the diameter of the grids:

$$\Delta L = \frac{1}{2}\int_0^L \left(\frac{dw}{dx}\right)^2 dx = \frac{\pi^2 w_m^2}{4L} \tag{19}$$

The shear displacement caused by shear stress should be considered. When a thermal expansion occurs in the grids with edge fixed support, the edge area is influenced by opposite shear stress. With the assumption that the fixed areas of the grids only have tangential stress, and since the grids are approximated as a flat plate (with a rectangular cross-section), the shear displacement of the grid can be approximately replaced by the shear displacement of a truss. Based on Hooke's law, as shown in Eq. 20, the shear displacement is expressed as γ, where τ and G are shear stress and shear modulus, respectively, and A is the section of the shear surface (Sun and Fang 2012):

$$\gamma = \frac{\tau}{G} = \frac{4\alpha T(r)(1+\mu)}{AE} \tag{20}$$

Substituting the coefficients of the grids, it can be calculated that the maximum deflection w_m of the screen grid is 1.145 mm, and the maximum radial prolongation ΔL is 0.008 mm. Meanwhile, the maximum deflection of the accelerator grid is 0.665 mm, and the gap between the screen grid and the accelerator grid decreases to 0.480 mm when the ion thruster is operated in steady status. To verify the accuracy of the calculation results, a thin plate FEM model with edge fixed support is built, and the size of the model is the same as that of the actual grid structure, that is, the thickness is 0.5 mm and the radius is 150 mm. In addition, the mechanical properties of the model are set as the equivalent elastic modulus of a flat plate without holes (shown in Table 1). The edge of the model is set as a fixed support, meaning that the degrees of freedom at the edge of the grids are fixed, which is consistent with the fixed installation method of the actual grid edge. The temperature boundaries are based on the previous calculation results. The thermal deformation in the Z direction and X direction of the screen grid are shown in Fig. 9a and b. The maximum deformation of the screen grid in the Z direction is 1.255 mm, and the maximum deformation of the screen grid in the X direction is 0.010 mm. Meanwhile, the maximum deformation of the accelerator grid in the Z direction is 0.723 mm, which is in accordance with the theoretical results.

Hot grid gap test results

To verify the accuracy of the calculation results of the hot grid gap, a hot gap experiment is conducted in this paper. As shown in Fig. 10a, an alumina ceramic probe with the largest diameter of 8 mm (height 2 mm) and a smallest diameter of 0.8 mm (height 4 mm) is fabricated. There are three through-holes with a diameter of 1 mm on the probe, and the angle between each hole is 120°. The probe is fixed to the screen grid by a thin steel wire, and the probe rod extends out of the accelerator grid. Meanwhile, the probe is designed to have a small thermal mass to reduce the influence on the experimental results.

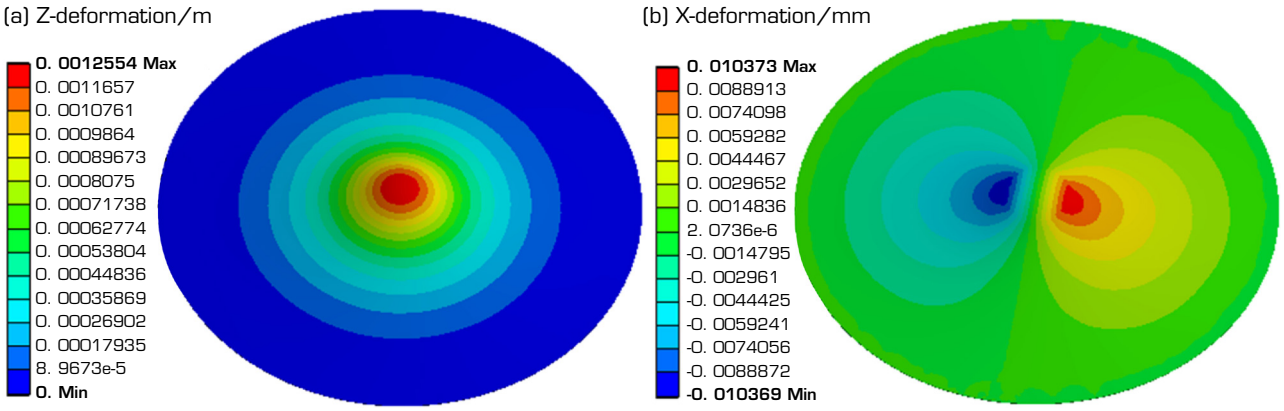

Source: Elaborated by the authors.

Figure 9. Thermal deformation of the screen grid. (a) Z-directional thermal deformation of the screen grid; (b) X-directional thermal deformation of the screen grid.

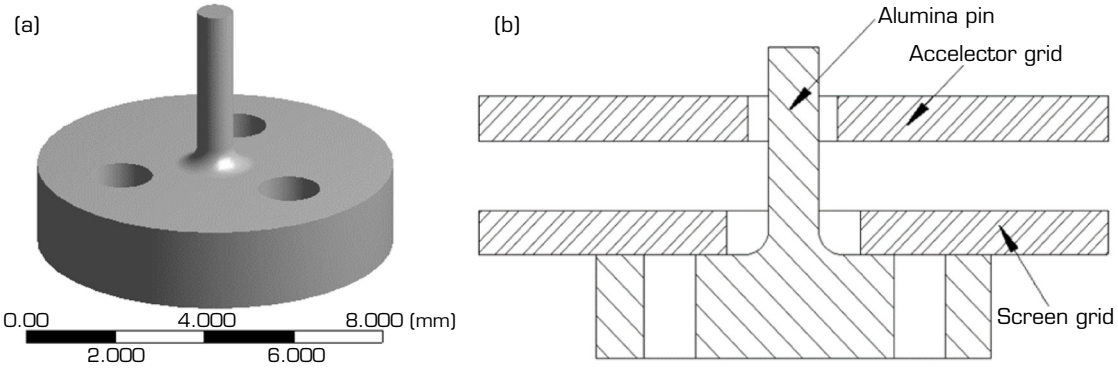

Source: Elaborated by the authors.

Figure 10. Structure and installation of the probes in the hot gap test. (a) structure of the probe; (b) ceramics probe fixed to the screen grid.

A high-magnification AVT camera and an Mk-APO-CPN4.0/60 lens are used for the grid hot gap test, and the grid gap variation can be obtained from the position change of the probe. In the test, the camera is covered with aluminium foil to prevent heat radiation from the thruster to the camera and enable the camera to operate normally in a plasma environment (Jia *et al.* 2012; Zhong *et al.* 2010).

To measure the grid gap variation, a thin steel wire is used to fix the probe on the screen grid. Compared with the screw fixation method, the screw head holding the probe is inserted between the two grids and occupies about 0.28 mm of the grid gap, which affects the measurement range of the grid gap. In the test, the 30 cm diameter ion thruster is operated under a 5 kW rated condition without beam extraction (Sun *et al.* 2014). Then, based on the high magnification camera, two photographs are captured, respectively, during the initial operation and stable operation (about 2 hours) of the thruster, respectively. By comparing the positions of the probe before and after in the two images, the change in the grid gap can be obtained. Fig. 11a shows that the probe is installed on the screen grid and the pinhead protrudes out of the aperture of the accelerator grid. In addition, Fig. 11b shows the position of the pinhead after the thruster has been operating for 2 hours without beam extraction (the temperature has reached equilibrium).

The test results show that the position change of the pinhead is in the range of 0.502 ~ 0.553 mm, and the measurements are close to the theoretical results (which are calculated to be 0.480 mm). The comparison results show that the theoretical calculation

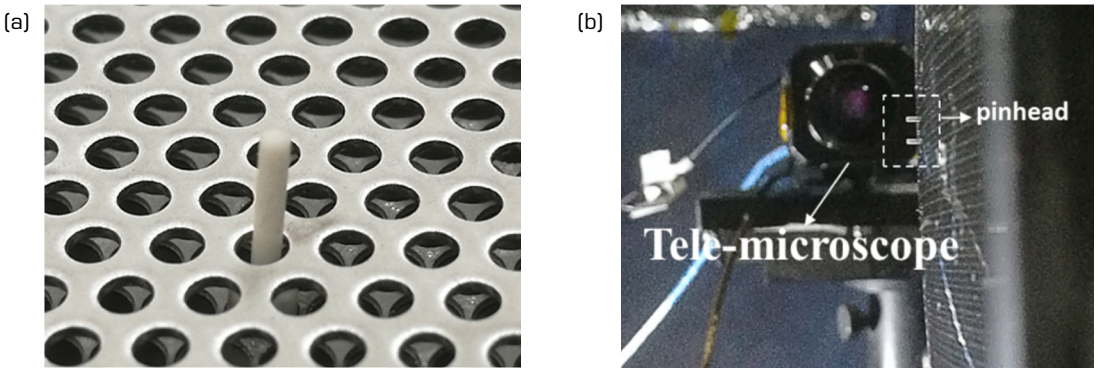

Source: Elaborated by the authors.

Figure 11. Probe position in the hot gap test. (a) pin head extends out of the grid surface; (b) pin head position after 2 hours of operating.

process is correct, and it can be used to estimate the thermal deformation of the grid gap variation of the ion thruster, with high accuracy. Moreover, it should be noted that the grid gap is measured without beam extraction, while the theoretical analysis result of the grid gap is obtained with beam extraction. According to previous thermal tests of the ion thrusters, under both with beam extraction and no beam extraction conditions, the temperature differences at the edges of the grids are not significant. Therefore, the theoretical calculation results can be approximately used to reflect the variation in grid gap when the thruster is operating under beam extraction.

CONCLUSION

By using the material mechanics analysis method, the material properties of the grids of a 30 cm diameter ion thruster have been equivalently treated and verified, and the equivalent error is estimated in this paper. In addition, the simulated thermal deformation of the grids is verified by the grid hot gap test. The research results show that after the equivalent treatment, the elastic modulus of the screen grid is 20.792 MPa with an equivalent coefficient of 0.741, and the elastic modulus of the accelerator grid is 89.435 MPa with an equivalent coefficient of 0.192. The thermal deformation of the plate grid with edge unconstrained is mainly caused by tensile stress in the horizontal direction; however, the deformation in the normal direction can be ignored. For the edge-constrained plate grids, the maximum deflection appears in the center of the grids. The maximum deflection is 1.145 mm for the screen grid and 0.665 mm for the accelerator grid. In addition, the simulated grid gap variation is 0.480 mm. The hot gap test results show that the grid gap changes from 0.502 mm to 0.553 mm when the thruster reaches thermal equilibrium, and the test results are in agreement with the simulation results.

CONFLICTS OF INTEREST

Nothing to declare.

AUTHOR CONTRIBUTIONS

Conceptualization: Sun M; **Methodology:** Sun M; **Software:** Sun M; **Validation:** Sun M; **Formal analysis:** Sun M and Ma Y; **Investigation:** Kong F; **Resources:** Sun M and Kong F; **Data Curation:** Sun M; **Writing - Original Draft:** Sun M; **Writing - Review & Editing:** Sun M; **Supervision:** Sun M and Kong F; **Final approval:** Sun M.

DATA AVAILABILITY STATEMENT

The data that support the findings of this study are available from the corresponding author upon reasonable request.

FUNDING

Key Talent Project of Gansu Province of China
Grant No. 2025RCXM034

Joint horizontal research projects between schools and enterprises
Grants No. LWL-KJ-2024-053 and No. LWL-KJ-2025-048

DECLARATION OF USE OF ARTIFICIAL INTELLIGENCE TOOLS

No artificial intelligence tools are used in the research and writing of this article.

ACKNOWLEDGEMENTS

Not applicable.

REFERENCES

Cao G, Wang GZ, Ren XR (2005) Fundamental solution to one-dimensional heat conduction equation. J Shandong Inst Light Ind 19(4):77-80. https://doi.org/10.3969/j.issn.1004-4280.2005.04.017

Diaz M, Soulas G (2006) Grid gap measurement for an NSTAR ion thruster. Paper presented 2006 29th International Electric Propulsion Conference. Electric Rocket Propulsion Society; Princeton, USA. https://www.mendeley.com/catalogue/46716d42-119f-3082-b65e-da9bfb72950d/

Gao QF, Zhang YS, Wang LB, Zuo G (2008) Finite element analysis of ion thruster grid subassembly based on homogenization method. Vac Cryogen 14(1):45-52. https://doi.org/10.3969/j.issn.1006-7086.2008.01.011

Gatewood B (1957) Thermal stresses with applications to airplanes, missiles, turbines, and nuclear reactors. New York: McGraw-Hill Book Inc.; p. 197-198.

Goebel D, Katz I (2008) Fundamentals of electric propulsion: ion and Hall thrusters. JPL space science and technology series. Hoboken: John Wiley & Sons; p. 206-207.

Haag T, Soulas G (2002) Performance of 8 cm pyrolytic-graphite ion thruster optics. Paper presented 2002 39th AIAA/ASME/SAE/ASEE Joint Propulsion Conference and Exhibit. American Institute of Aeronautics and Astronautics; Huntsville, USA. https://doi.org/10.2514/6.2003-4557

Haag T, Soulas G (2003) Performance and vibration of 30 cm pyrolytic ion thruster optics. Paper presented 2003 39th Joint Propulsion Conference and Exhibit. American Institute of Aeronautics and Astronautics; Huntsville, USA.

Hassani B, Hinton E (1999a) A review of homogenization and topology optimization I – Homogenization theory for media with periodic structures. Comput Struct 69(9):707-717. https://www.sciencedirect.com/science/article/abs/pii/S004579499800131X?via%3Dihub

Hassani B, Hinton E (1999b) A review of homogenization and topology optimization II – Analytical and numerical solution of homogenization equations. Comput Struct 69(9):719-738. https://www.sciencedirect.com/science/article/abs/pii/S0045794998001321?via%3Dihub

Hassani B, Hinton E (1999c) A review of homogenization and topology optimization III – Topology optimization using optimality criteria. Comput Struct 69(9):739-756. https://www.mendeley.com/catalogue/6c568993-90d6-3034-935f-36de40d30cd4/

Jia YH, Zhang TP, Zheng MF, Li XK (2012) Numerical analysis for electron backstreaming accelerator grid limited voltage for 20 cm Xe electric propulsion thruster grid system. J Propuls Technol 33(6):991-996. https://d.wanfangdata.com.cn/periodical/tjjs201206026

Liu WY, Yang J, Mao GW, Li KZ (2007) Mechanical property evaluation of C/C composite material grids for electron cyclotron resonance thruster. J Propuls Technol 28(6):692-696. https://d.wanfangdata.com.cn/periodical/CiBQZXJpb2RpY2FsQ0hJU29scjkyMDI2MDExMjE3MDQyNhINdGpqczIwMDcwNjAyMhoIamdrbHVrZWo%253D

MacRae G, Zavesky R, Gooder (1982) Structural and thermal response of 30 cm diameter electric propulsion thruster optics. Paper presented 1982 25th Joint Propulsion Conference and Exhibit. American Institute of Aeronautics and Astronautics; Monterey, USA. https://doi.org/10.2514/6.1989-2719

Meckel N, Polaha J (2004) Structural analysis of pyrolytic graphite optics for the HiPEP electric propulsion thruster. Paper presented 2004 40th Joint Propulsion Conference and Exhibit. American Institute of Aeronautics and Astronautics; Fort Lauderdale, USA. https://doi.org/10.2514/6.2004-3629

Mueller J, Brophy J, Brown D (1995) Endurance testing and fabrication of advanced 15-cm and 30-cm carbon-carbon composite grids. Paper presented 1995 31st Joint Propulsion Conference and Exhibit. American Institute of Aeronautics and Astronautics; San Diego, USA. https://doi.org/10.2514/6.1995-2660

Soulas G (2006) Calculation of thermally induced displacements in spherically domed ion engine grids. Paper presented 2006 29th International Electric Propulsion Conference. Electric Rocket Propulsion Society; Princeton, USA. https://www.mendeley.com/catalogue/2b3869a0-9c36-3ebf-948f-25b7ed0e61d1/

Soulas G, Frandina M (2004) Ion engine grid gap measurements. Paper presented 2004 40th Joint Propulsion Conference and Exhibit. American Institute of Aeronautics and Astronautics; Fort Lauderdale, USA. https://doi.org/10.2514/6.2004-3961

Sun MM, Qi XF (2023) Hot gap measurement of a three-grid system for a 30 cm diameter ion thruster with beam extraction. IEEE Trans Plasma Sci 51(10):3053-3061. https://doi.org/10.1109/TPS.2023.3319534

Sun MM, Zhang TP, Wang L (2014) Thermal analysis of 30 cm diameter thruster. Vac Cryogen 20(3):158-162. https://dx.doi.org/10.3969/j.issn.1006-7086.2014.03.008

Sun XF, Fang XS (2012) Mechanics of materials. 3rd ed. Beijing: Higher Education Press; p. 239-240.

Wen Z, Zhong LW, Wang YB, Ren J (2011) Three-dimensional numerical study on motion laws of ions in electric propulsion thruster optics. High Power Laser Part Beams 24(10):1640-1645. https://doi.org/10.3788/HPLPB20112306.1640

Zhong LW, Liu Y, Li J, Gu Z, Jiang HC, Wang HX, Tang HB (2010) Numerical simulation of characteristics of CEX ions in electric propulsion thruster optical system. Chin J Aeronaut 23:15-21. https://doi.org/10.1016/S1000-9361(09)60182-5